J. Fluid Mech. (2010), *vol.* 651, *pp.* 117–143.
doi:10.1017/S0022112009993788

Instability of a viscous liquid coating a cylindrical fibre

ALEJANDRO G. GONZÁLEZ[1]†, JAVIER A. DIEZ[1], ROBERTO GRATTON[1], DIEGO M. CAMPANA[2,3] AND FERNANDO A. SAITA[2]

[1]Instituto de Física Arroyo Seco, Universidad Nacional del Centro de la Provincia de Buenos Aires, Pinto 399, Tandil, Argentina

[2]INTEC-CONICET, Universidad Nacional del Litoral, Güemes 3450, Santa Fe, Argentina

[3]Facultad de Ingeniería, Universidad Nacional de Entre Ríos, Ruta 11 (Km. 10), Oro Verde, Entre Rríos, Argentina

(Received 26 February 2009; revised 27 November 2009; accepted 3 December2009; first published online 22 March 2010)

The instability of a liquid layer coating the surface of a thin cylindrical wire is studied experimentally and numerically with negligible gravity effects. The initial uniform film is obtained as the residual of a sliding drop, and the thickness measurements are performed with an anamorphic optical system that compresses the vertical scale (allowing to observe several wavelengths) and widens the horizontal one (to follow in detail the evolution of local minima and maxima). Experimental timelines showing the growth and position of the maxima and minima are compared with linear theory and fully nonlinear simulations. A primary mode grows in the early stages of the instability, and its wavelength λ_1 is not always in agreement with that corresponding to the maximum growth rate predicted by the linear theory λ_m. In later stages, a secondary mode appears, whose wavelength is half that of the primary mode. The behaviour of the secondary mode allows us to classify the experimental results into two cases, depending on whether it is linearly stable (case I) or unstable (case II). In case I, the amplitude of the secondary mode remains small compared with that of the primary one, while in case II both amplitudes may become very similar at the end. Thus, the distance between the final drops may be quite different from that seen between initial protuberances. The analysis of the experiments allows us to define a simple criterion based on the comparison between λ_1 and λ_m. Contrary to the predictions of widely used previous quasi-static theories, experiments show that the relation between maximum and minimum of the primary mode is better approximated by a kinematic model based on the assumption that primary maxima increase as fast as the minima decrease. Numerical simulations confirm this hypothesis.

1. Introduction

The problem of coating a cylindrical fibre with a liquid film has been widely investigated because of its relation with industrial and technological processes, such as the coverage of conducting cables with isolating films and lubrication of glass or polymeric fibres to prevent rupture during manipulation. In most of these applications, the coating is obtained by vertical withdrawal of the fibre from a liquid bath. An

† Email address for correspondence: aggonzal@exa.unicen.edu.ar

important issue of this process is the dependence of the thickness of the coating film with the withdrawal speed, fibre radius and physico-chemical parameters of the liquid. Extensive reviews on these aspects of the problem can be found in Quéré (1999) and Weinstein & Ruschak (2004). After the film is formed, a Plateau–Rayleigh-type instability (Plateau 1873; Rayleigh 1879, 1892) takes place, which might lead to the breakup of the film and subsequent formation of beads. In some applications, the instability is stopped by means of a fast cooling and solidification of the coating, but in other technological procedures this is not possible. Therefore, it is relevant to understand the mechanisms that govern this instability, its time scale and general dependence on the various parameters.

When the fluid radius is small enough, gravity effects can be neglected and only viscous, capillary and possibly inertial forces govern the flow. Under these conditions, Goren (1962) performed a linear stability analysis of Navier–Stokes equations and determined that only wavelengths larger than the perimeter of the liquid–air interface are unstable. He also found analytical expressions for the growth rates of perturbations as a function of the wavelength for the limiting cases of Stokes and inviscid flows. His experiments showed a reasonable agreement with his theory when comparing the wavelength of maximum growth rate with the final distance between beads. In a subsequent work, Goren (1964) developed a quasi-static model to calculate the shape of the interface during the evolution. He assumed that the free surface shape is a series of maxima (bulges) connected by flat cylindrical zones of constant thickness and minimized the surface energy of that configuration. This model does not include secondary maxima (or satellite beads) also observed in his experiments. Almost a decade later, Carroll & Lucassen (1974) studied experimentally and theoretically the slowdown of the instability due to the presence of a surfactant. More recently, Yarin, Oron & Roseneau (1993) studied the flow by using balance equations of mass, momentum and energy integrated across the liquid thickness using lubrication approximation. Their numerical simulations showed that nonlinear interaction of linearly stable modes leads to the formation of secondary maxima in between the primary ones. Recently, Lister *et al.* (2006) studied the long-time dynamics of primary and secondary beads formed as a consequence of the instability. In this case, the gradient of capillary pressure drives the slow drainage between beads. These authors numerically solved the evolution equation for thin films and found different behaviours depending on the axial lengths of the structures.

When gravitational effects are *not negligible* and the fibre is in vertical position, the induced axial flow interacts with the capillary instability. Among the pioneer works for this case are those of Goucher & Ward (1922) and Kapitza & Kapitza (1964). Several other authors, such as Lin & Liu (1975) and Krantz & Zollars (1976), performed the linear stability analysis of simplified models for thin coating films and/or long wavelengths. Solorio & Sen (1987) numerically solved the Orr–Sommerfeld equation for this problem. Thus, they were able to carry out a linear stability analysis with no restrictions on the wavenumber, Reynolds number, Re, or film thickness. Their results show that the cylindrical film is unstable for all Re, Weber number, We, and fluid thickness. Moreover, as both Re and We increase, the wavenumber of the most unstable mode decreases for thicker films and increases for thinner ones. In the same year, Frenkel *et al.* (1987) reported theoretical evidence that Plateau–Rayleigh instability can saturate in a certain range of parameters when it interacts with gravitational flow. Quéré (1990) experimentally studied thin films on thick fibres and found a critical fluid thickness below which the interfacial undulations due to

this instability are not visible any more on the gravitational base flow. This critical thickness scales as the cube of the fibre radius and does not depend on the fluid viscosity. With the parameters of our experiments, this critical thickness is of the order of 0.1 μm. Quéré worked with fibre radius, R, much larger (80 μm $\leqslant R \leqslant$ 400 μm) than those used here. His findings were theoretically studied later by Kalliadasis & Chang (1994).

Among the most recent works on this subject, we can mention Kliakhandler, Davis & Bankoff (2001), who investigated experimentally and theoretically the dynamics of a thick fluid film flowing down vertically on a thin fibre at constant flow rate. Depending on its magnitude, these authors determined three possible patterns for the drops flowing down the fibre. They also derived and numerically solved a simplified evolution equation for long wavelengths and dominant capillary effects ($Ca \to 0$). However, this model was not able to describe the drops pattern for large flow rates. This limitation was removed by Craster & Matar (2006), who modelled the problem under the assumption that the interfacial radius is much less than the capillary length. They considered small Bond number and the Reynolds number in such a way that its effective value is small enough to yield negligible inertial contributions. More recently, we can mention the works by Duprat *et al.* (2007) and Smolka, North & Guerra (2008), where linear theories developed by Kliakhandler *et al.* (2001), Craster & Matar (2006) and Trifonov (1992) are compared with experiments. Analogous to the measurements reported here, they are concerned with the wavelengths and growth rates of the modes in their instability problem (which can be convectively or absolutely unstable), where the beads travel down the fibre. In spite of the large body of research done on the instability of films deposited on cylindrical fibres, there are still few experimental data to undoubtedly support the theoretical predictions.

In the particular case of *negligible* gravitational effects, which is in the scope of this work, we can only mention the experiments carried out by Goren (1962, 1964), Carroll & Lucassen (1974) and, more recently, de Bruyn (1997). Even though Mashayek & Ashgriz (1995) reported a complete work on the numerical simulation of this problem, they did not compare their predictions with any experimental data. Therefore, the aim of our work is twofold. On the one hand, we report experimental results that allow us to follow the time evolution of the interface, so that main features of the instability can be measured, such as growth rates and dominant wavelengths. The experimental set-up is similar to that of Goren (1964), but uses an anamorphic optical system to increase the resolution of the liquid thickness. On the other hand, we also present direct numerical simulations of Navier–Stokes equations, whose results are compared with the experimental data. The numerical code is an adaptation of a previously validated one by Campana, Di Paolo & Saita (2004).

This paper is organized as follows. In § 2 we describe the experimental set-up and the optical techniques used to investigate the instability. The results of a series of experiments are grouped into two cases that distinguish typical evolutions of the instability. In § 3 we revisit the linear stability results in order to compare the observed primary and secondary wavelengths with that of the maximum growth rate of the theory, as well as the corresponding experimental and theoretical growth rates. In § 4 we attempt to describe the experimental free surface evolution with the quasi–static model developed by Goren (1964). Section 5 is devoted to the presentation of the numerical predictions and their comparison with experimental results and § 6 includes a discussion on the role played by the initial conditions of the problem.

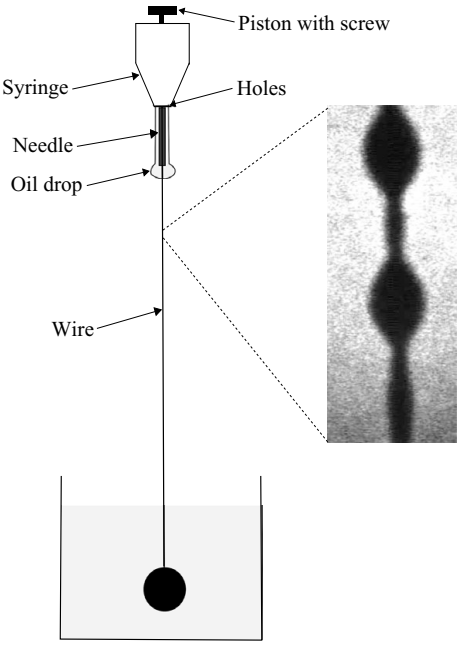

(*a*) Experimental set-up

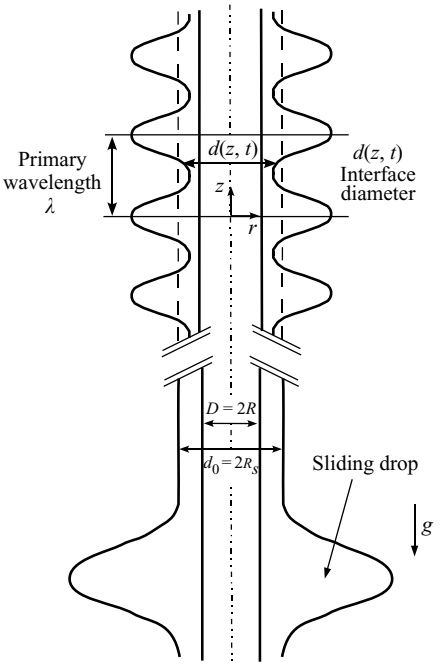

(*b*) Sketch of the instability

FIGURE 1. (*a*) Experimental set-up. The oil in the syringe is pushed through the holes, and a symmetrically threaded drop is formed at the tip of the needle. As the drop slides down, a thin film is left behind. The inset is a picture of the actual final stage without anamorphic distortion. Note that the lower and upper parts of the drop are symmetric because gravity effects are negligible. (*b*) Sketch of the anamorphic view of the instability showing the main parameters of the problem (the variables correspond to real undistorted values).

2. Experiments

The device consists of a copper wire (diameter $D = 110$ μm) vertically suspended and tightly threaded through the needle of a syringe (see figure 1*a*). The cap holding the needle has a series of lateral small holes through which silicon oil (polydimethylsiloxane (PDMS) of viscosity $\mu = 11$–23 poise, density $\rho = 0.96$ g cm^{-3} and surface tension $\sigma = 24$ dyn cm^{-1}) is pushed out by using a piston. Its movement and the amount of ejected liquid are smoothly controlled by an upper screw. The oil forms a thin film flowing down the needle till reaching its tip where a pinned drop grows around the wire and finally detaches. The drop is centred on the wire and slides along it by gravity. As the drop falls, a trail of oil is left behind. At a certain distance from the drop, the thickness of the film is practically uniform for a length of at least some millimetres along the wire. This system also ensures an azimuthally symmetric coating. The film thickness depends on the size of the drop, which in turn is controlled by the amount of fluid ejected by the syringe. The instability of this coating involves two quite different scales: the vertical one that corresponds to the typical wavelength, λ, of the surface perturbation and the horizontal one that characterizes the local diameter, $d(z, t)$, of the coating (see figure 1*b*).

An ordinary (homomorphic) optical system does not suffice to measure accurately both scales, because a large amplification of the horizontal scale, in order to allow a detailed study of the growth rate of the amplitude of the instability, leads to pictures

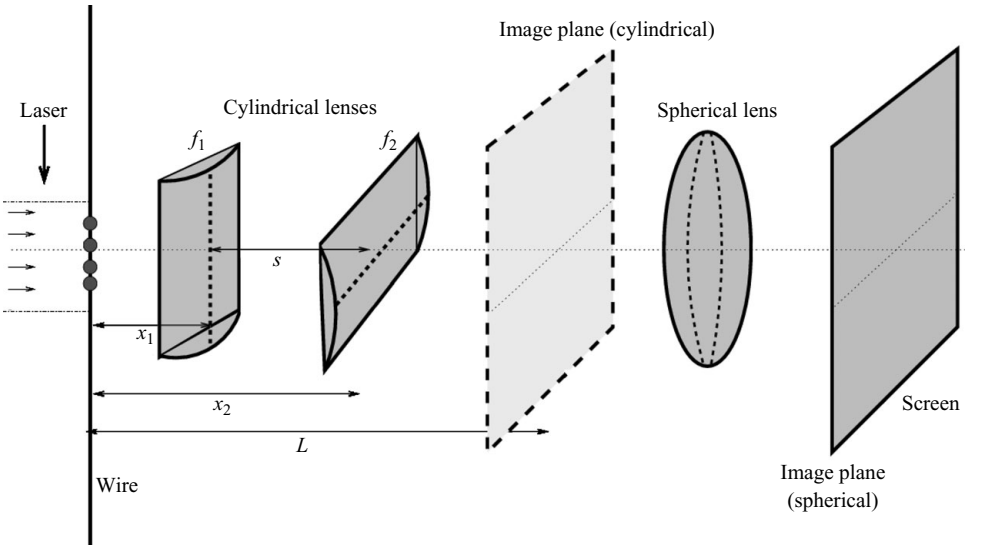

FIGURE 2. Anamorphic optical system used to study the evolution of the instability. It yields a horizontal amplification and a vertical compression of the image.

from which one cannot confidently determine the typical wavelength. Therefore, we use an anamorphic optical system that distorts the image by compressing the vertical scale in order to observe several wavelengths and widens the horizontal one (Collicott, Zhang & Schneider 1994). Thus, this system allows a quantitative study of the evolution of local minima and maxima.

The anamorphic system is formed by two cross cylindrical lenses separated by a distance $s = x_2 - x_1$ (see figure 2). The axis of the first lens is vertical, while the axis of the second one is horizontal. The positions of both lenses, x_1 and x_2, are given by

$$x_1 = \frac{L}{2}(1 - \Delta_1), \qquad x_2 = \frac{L}{2}(1 + \Delta_2), \tag{2.1}$$

where $\Delta_i = \sqrt{1 - 4f_i/L}$, f_i is the focal length of the ith lens and L is the distant between the object plane (which contains the coated wire) and the image plane. The ratio between the horizontal magnification of the first lens and the vertical magnification of the second one measures the anamorphism, $\mathscr{A}$, of the optical system:

$$\mathscr{A} = \frac{(1 + \Delta_1)(1 + \Delta_2)}{(1 - \Delta_1)(1 - \Delta_2)} \tag{2.2}$$

Note that the horizontal and vertical processes of image formation, and consequently the magnifications, are independent one of another within the paraxial approximation assumed here. The resulting image is further amplified in an homomorphic way by using a spherical lens. The image formed on a distant screen is digitally recorded as a video movie at a rate of 29.97 f.p.s. Each frame size is 352×240 pixels. In our system, we choose an anamorphism of $\mathscr{A} = 11.6$ by using two lenses with $f_1 = f_2 = 12.5$ cm and $L = 71.3$ cm. The choice of this value of $\mathscr{A}$ is guided by the fact that the observed wavelengths are of the order of 1 mm, while the typical fluid thickness is around 0.1 mm. This means that the size of a single pixel is about 32 μm in the vertical direction and 2.9 μm in the horizontal one. Consequently, it is easy to estimate the error for vertical and horizontal distances, because its digital uncertainties are within one or two pixels.

An important dimensionless parameter of the problem is $F=(d_0-D)/D$, where d_0 $(=2R_s)$ is the initial diameter of the free surface of the coating left by the sliding drop, and D $(=2R)$ is the diameter of the wire.

In order to ensure negligible effects of gravity, two issues should be taken into account. In the first place, the pressure variation due to gravity along a wavelength λ should be negligible with respect to the capillary pressure, i.e. $\rho g\lambda \ll \sigma/R_s$. This condition is fulfilled for Bond number $Bo=(R_s/a)^2 \ll R_s/\lambda$, where $a=\sqrt{\sigma/(\rho g)}$ is the capillary distance. This is a necessary, but not sufficient, condition to have symmetrical drops in the sense that the upper and lower parts have similar shapes resulting from the instability. Second, the capillary number $Ca=\mu U/\sigma$, given by the vertical drift velocity U, must be very small to achieve this symmetry. This condition ensures that the fluid has basically no vertical motion during the evolution of the instability. Assuming a balance between gravitational and viscous forces, i.e. $2\pi\mu U/F=\pi\rho g(R_s^2-R^2)$, we obtain the following relationship between Ca and Bo:

$$Ca=\frac{F^2(F+2)}{2(F+1)^2}Bo. \tag{2.3}$$

Because we perform experiments with F in the range $0.4<F<3.25$, and $Bo\approx 0.01$, the condition $Ca\ll 1$ is satisfied. Note that the experiments of Kliakhandler *et al.* (2001) are carried out in a different regime, in which the final drops are asymmetrical in the z direction, showing differences in the upper and lower portions, and an important vertical flow is present in the drop motion.

Here, we perform a series of experiments for different values of F and μ (see table 1). Because $Ca\ll 1$, the value of μ only determines the time scale of the instability and it does not significantly affect either the dynamics or the resulting pattern. Therefore, viscosity does not characterize the cases presented below. The variation of F is due to different sizes of the sliding drop that generates the initial film, while keeping constant the wire diameter. In all the experiments we distinguish two characteristic behaviours, which we classify as cases I and II (see the last column of table 1). Case I includes the experiments whose secondary peak does not grow by itself, but only due to decreasing of the absolute minimum. In other words, this peak represents a linearly stable mode. Instead, the experiments in case II have a secondary peak which effectively grows, thus behaving as an unstable linear mode. For brevity, we consider in detail one experiment each case as representatives of typical evolutions of the instability. When appropriate, results of the whole series of experiments are also reported.

2.1. *Case I: stable linear secondary mode*

In this section, we choose experiment 8 ($F=1.73$, $\mu=23$ poise) as a representative of case I. Figure 3 shows snapshots of the evolution of the free surface. At $t=0$, the rear part of the sliding drop (bottom of the photo) and the resulting trailing film is observed in the picture. Two seconds later, a sinusoidal corrugation appears in the upper part of the film with a typical local wavelength λ_1, which we call primary wavelength. As the amplitude of this perturbation grows, the size of the perturbed region in the vertical (axial) direction also increases. The distance between maxima is roughly λ_1. Later on, secondary local maxima arise between the primary ones ($t=4.7$ s). A new typical wavelength, λ_2, is defined as the distance between adjacent primary and secondary peaks. Finally, all amplitudes saturate and the distances λ_1 and λ_2 characterize the whole pattern. Figure 3 shows that the average distance between secondary and primary maxima, λ_2, is approximately half of λ_1.

Experiment	F	μ (poise)	λ_1(mm)	λ_2(mm)	λ_1/λ_m	λ_2/λ_c	$2\lambda_c/\lambda_m$	Case
1	3.25	11.8	2.57	1.19	1.09	0.81	1.27	I
2	3.01	23.0	3.41	1.86	1.55	1.34	1.26	II
3	2.59	23.0	3.43	1.83	1.75	1.47	1.28	II
4	2.47	11.8	3.19	1.57	1.69	1.31	1.30	II*
5	2.33	23.0	3.41	1.75	1.89	1.52	1.33	II
6	1.94	11.8	2.31	1.20	1.47	1.19	1.39	II
7	1.73	23.0	1.40	0.80	0.97	0.85	1.37	I
8	1.73	23.0	1.28	0.55	0.89	0.58	1.37	I*
9	1.46	11.8	1.49	0.82	1.15	0.97	1.40	I
10	1.29	11.8	1.40	0.73	1.17	0.92	1.36	I
11	1.25	23.0	1.24	0.53	1.06	0.68	1.33	I
12	1.19	23.0	1.67	0.97	1.46	1.29	1.37	II
13	0.77	23.0	1.12	0.52	1.24	0.84	1.30	I
14	0.66	23.0	0.84	0.46	1.00	0.80	1.32	I
15	0.66	23.0	0.75	0.44	0.90	0.77	1.31	I
16	0.61	23.0	1.17	0.58	1.44	1.03	1.29	II
17	0.38	23.0	1.64	0.90	2.39	1.89	1.25	II
18	0.21	23.0	0.81	0.40	1.37	0.95	1.27	II

TABLE 1. Dimensionless film thickness and viscosity of each experiment, together with the measured distances between primary (λ_1) and secondary (λ_2) peaks. The values of λ_c and λ_m are the wavelengths of the critical (marginal instability) mode and that of the maximum growth rate as given by the linear theory, respectively. The asterisk (*) indicates experiments reported in detail.

In order to quantitatively describe the time evolution of the system, we follow the diameter of (a) a primary peak d_1, (b) a contiguous secondary peak d_2 and (c) the absolute minimum, d_{min}, in between. In figure 4, we plot the timelines of these diameters. Note that the secondary maximum is not an actual increase of the secondary peak, but its importance is due to the fast decrease of d_{min}. The timelines also show that the secondary maximum shows up at the beginning of the saturation stage of the primary maximum.

Note also that the value of λ_1 selected by the system is not univocally given by F, but it can vary around 10 % (see experiments 7 and 8 as well as 14 and 15 in table 1). Moreover, experiments with very similar values of F and different viscosities can lead to similar variations of λ_1 (see experiments 10 and 11 in table 1). A more detailed analysis of the experiments is presented in § 3 in relation to the linear stability theory, taking into account the growth rates in the early stages of the instability.

2.2. *Case II: unstable linear secondary mode*

For this case, we choose experiment 4 ($F = 2.47$, $\mu = 11.8$ poise) for a detailed analysis. The corresponding snapshots are shown in figure 5. Though a similar behaviour to the preceding experiment is observed, two main differences arise. First, the amplitude of the secondary peak actually grows, not as an effect of the decrease of the adjacent minimum as in case I, but due to its intrinsic growth rate. As a consequence, the secondary peak reaches an amplitude comparable with the primary peak. Second, a tertiary peak appears between secondary and primary maxima in this experiment. Not all experiments in case II necessarily show a measurable tertiary peak.

The timelines of primary and secondary maxima as well as the minimum are shown in figure 6. Here, we add a tertiary maximum timeline. Note that the evolution of the secondary maxima strongly differs from that observed in the previous case

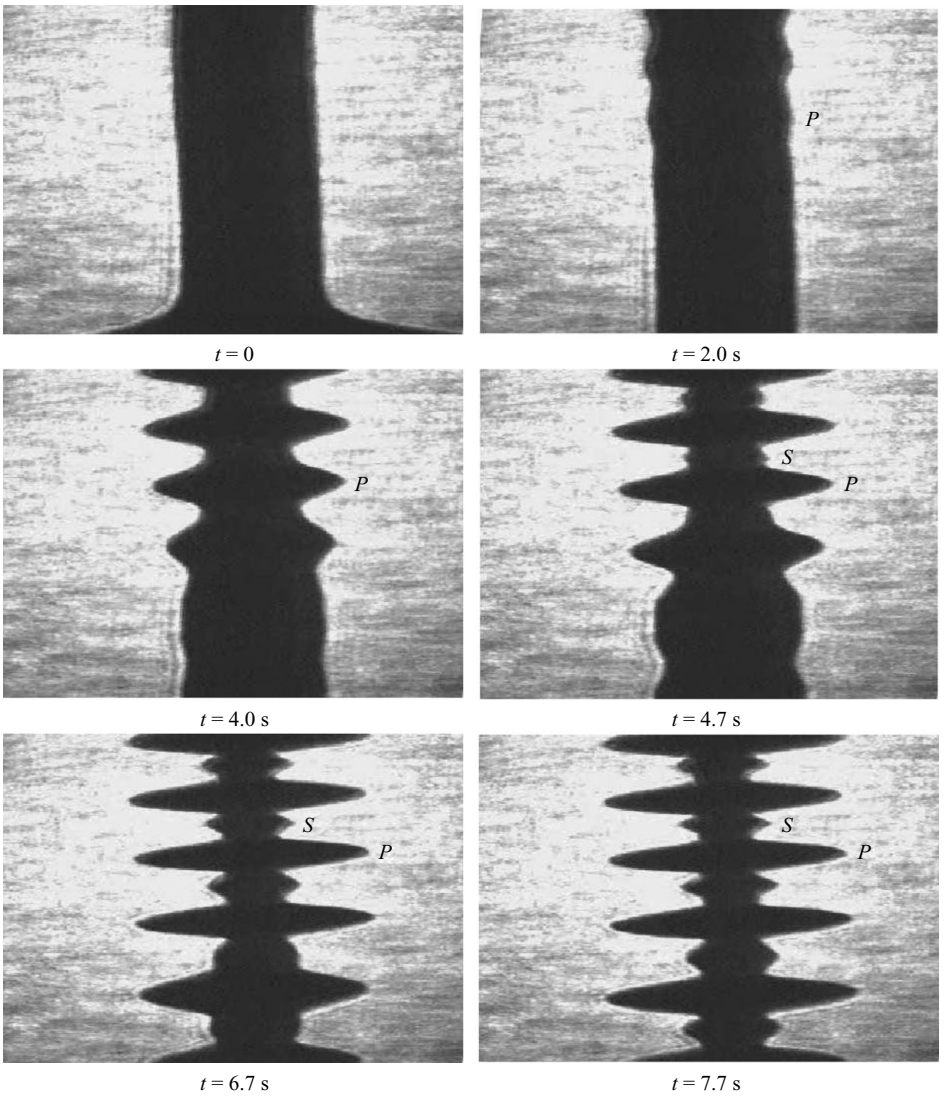

FIGURE 3. Time evolution of the instability in experiment 8 ($F = 1.73$, $\mu = 23$ poise) corresponding to case I. The letters P and S stand for the location of the primary and secondary peaks. The height and width of each picture correspond to 7.46 and 1.025 mm, respectively.

(cf. figure 6). Now, the local secondary peak starts growing when the primary mode begins to saturate. Almost simultaneously, a tertiary maximum appears without an actual increase of the thickness of the fluid there, while the absolute minimum keeps on decreasing. Therefore, the behaviour of the tertiary peak is analogous to that of the secondary peak in case I. The relation $\lambda_2 \simeq \lambda_1/2$ also holds in this case. Moreover, the distance between the tertiary and secondary peaks, λ_3, is approximately half that of λ_2.

In both cases, the instability evolves with no apparent vertical motion of the maxima. Nevertheless, after the last stages shown in figures 3 and 5, we observe that when the primary drops become big enough, they tend to slide down faster than the secondary and tertiary ones. As a consequence, the primary drops swallow the

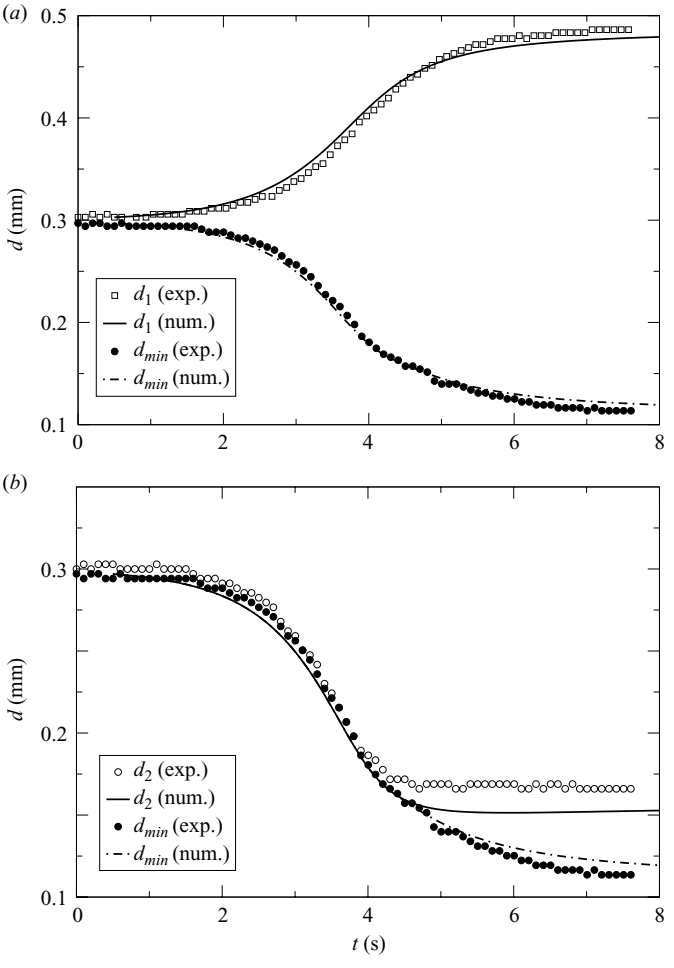

FIGURE 4. Comparison of timelines from experiment (exp.) 8 (case I) with the corresponding numerical simulation (num.) of Navier–Stokes equations (§ 5). (*a*) Primary peak, d_1, and nearby minimum, d_{min}; (*b*) secondary peak, d_2, and same minimum, d_{min}.

smaller drops, thus generating larger sliding drops. The study of this process is out of the scope of this paper. The description of this advanced stage (which includes coalescence of falling drops) is closer to the regime studied by Smolka *et al.* (2008).

In figure 7 we show the primary and secondary wavelengths measured in all experiments (see the fourth and fifth columns of table 1). The good fitting with the line $\lambda_2 = \lambda_1/2$ confirms the general validity of this pattern feature independent of the case. Note that the difference between cases I and II is not related to the viscosity, which only yields different time scales. The use of several values of μ does not modify the relationship between λ_1 and λ_2, as seen in figure 7.

2.3. *Growth rates of early stages*

Because the amplitude of the perturbations is small in the early stages of the instability, we plan to compare the measured growth rates in this stage with the linear theory developed by Goren (1962) (§ 3). With this aim, we plot the evolution of the thickness at the primary peak and define the amplitude of the perturbation as $A = (d_1 - d_{min})/d_0$.

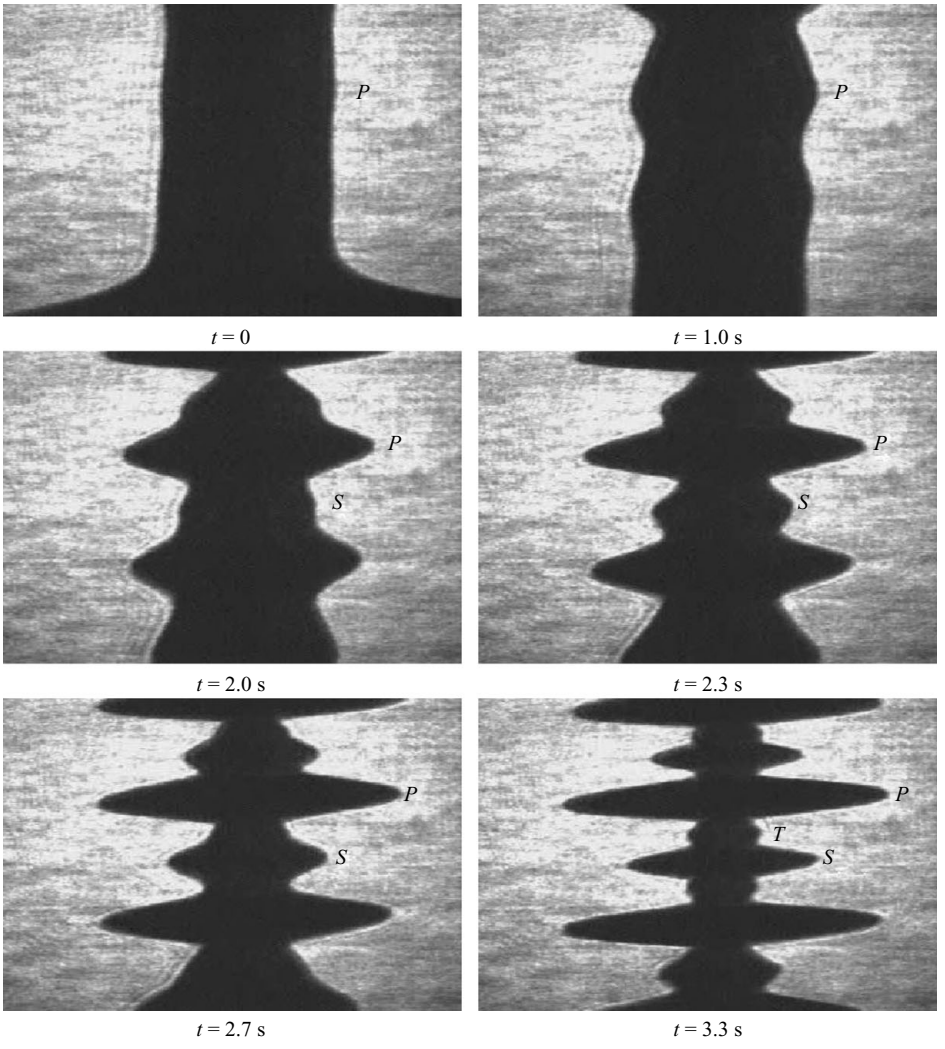

FIGURE 5. Time evolution of the instability in experiment 4 ($F = 2.47$, $\mu = 11.8$ poise) corresponding to case II. The letters P, S and T stand for the location of the primary, secondary and tertiary peaks, respectively. The height and width of each picture correspond to 8.01 mm and 1.015 mm, respectively.

Thus, we fit the early stages with an exponential function in order to measure the growth rates, γ_1^e. For instance, in figure 8(a) we show the evolution for experiments 8 (case I) and 4 (case II). As expected for later stages, nonlinear effects become important and the exponential behaviour (linear model) loses validity. Note that nonlinear effects modify this behaviour earlier in experiment 4 (case II) than in 8 (case I). In the fourth column of table 2 we report γ_1^e for the rest of the experiments.

Analogously, we proceed to calculate the corresponding growth rates of the secondary peak, by defining its amplitude as $A = (d_2 - d_{min})/d_0$ (see figure 8b).

3. Linear model

In order to have a framework for the understanding of the previous experimental results, here we revisit the linear model of the instability developed by Goren (1962).

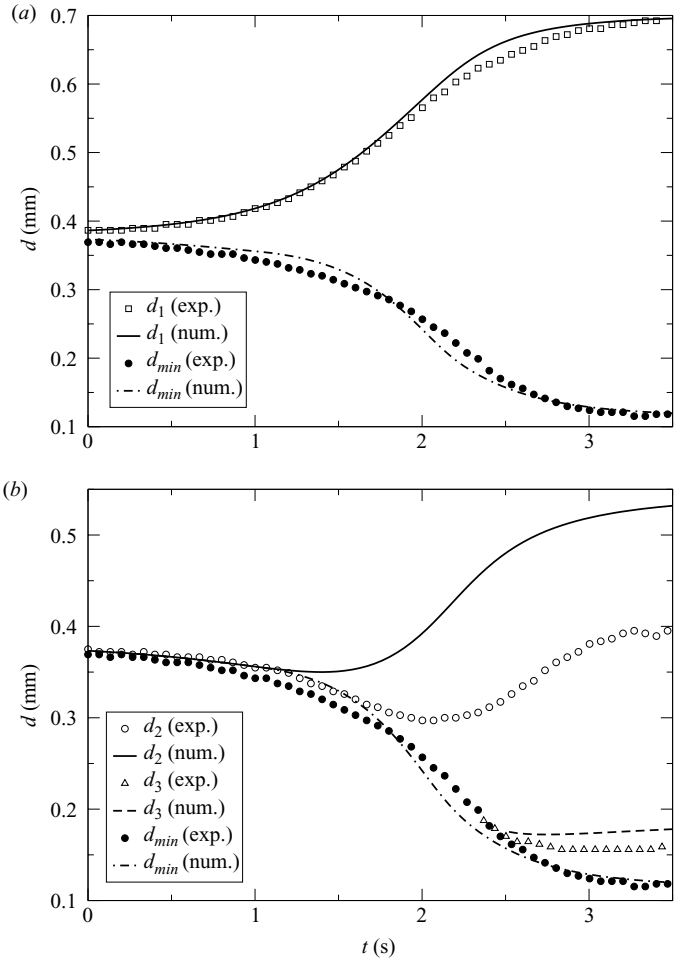

FIGURE 6. Comparison of timelines from experiment 4 (case II) with the corresponding numerical simulation of Navier–Stokes equations (§ 5). (*a*) Primary peak, d_1, and nearby minimum, d_{min}; (*b*) secondary peak, d_2, tertiary peak, d_3, and the same minimum, d_{min}. Symbols correspond to experimental data and lines show simulation results.

He assumes axially symmetric perturbations of an infinitely long coated wire of the form $\exp(\gamma t + \mathrm{i}kz)$, where $k = 2\pi/\lambda$ is the wavenumber. The unperturbed state corresponds to a fluid at rest and gravity effects are not considered. The dispersion relation is given by

$$\Gamma \equiv \gamma \frac{R_s \mu}{\sigma} = \frac{\frac{1}{2}(k^2 R_s^2 - 1)\Delta_1}{\Delta_2 + (k^2 R_s^2 + 1)\Delta_1}, \tag{3.1}$$

where

$$\begin{aligned}\Delta_1 = &-1 + 2kR\,[K_0(kR)I_1(kR_s) + I_0(kR)K_1(kR_s)] \\ &\times [K_1(kR)I_1(kR_s) - I_1(kR)K_1(kR_s)] \\ &+ (kR)^2\,[K_0(kR)I_1(kR_s) + I_0(kR)K_1(kR_s)]^2 \\ &- (kR)^2\,[K_1(kR)I_1(kR_s) + I_1(kR)K_1(kR_s)]^2\,,\end{aligned} \tag{3.2}$$

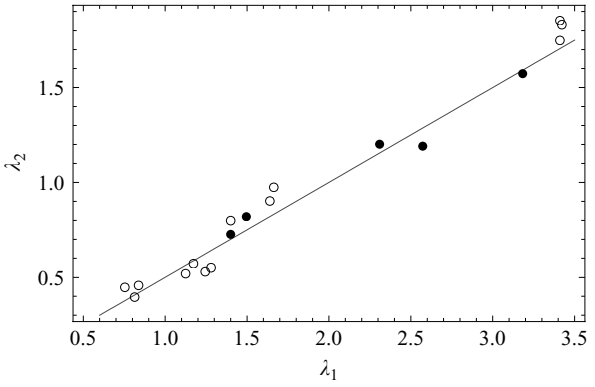

FIGURE 7. Wavelength of primary mode, λ_1, versus wavelength of secondary mode, λ_2, from a series of experiments with different values of F and μ. The open and close circles correspond to $\mu = 23$ poise and 11.8 poise, respectively. The values of F for each case can be seen in figure 10 (see also table 1). The solid line is $\lambda_2 = \lambda_1/2$.

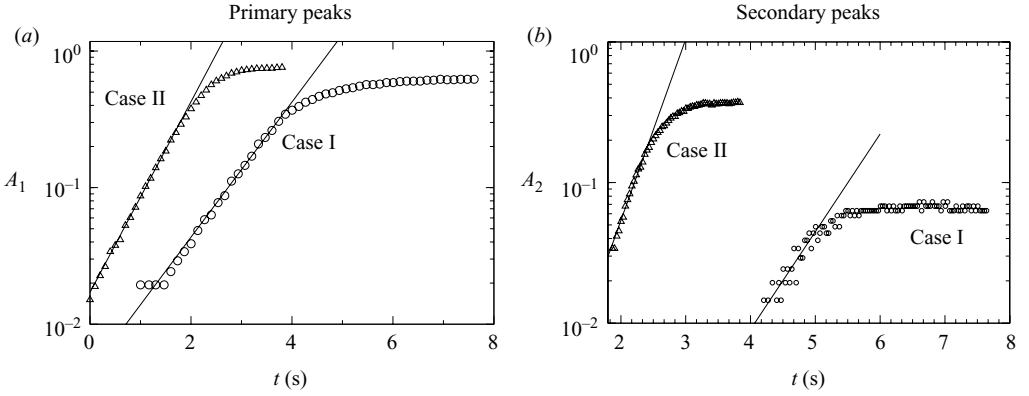

FIGURE 8. Time evolution of the amplitude of the modes for experiments 8 (case I, circles) and 4 (case II, triangles). The best fits for the early stages are given by the solid lines. (*a*) Amplitude, $A_1 = (d_1 - d_{min})/d_0$, of the *primary* mode. (*b*) Amplitude, $A_2 = (d_2 - d_{min})/d_0$, of the *secondary* mode.

and

$$\begin{aligned}\Delta_2 = &-(1 + k^2R^2) + 2k^3RR_s^2 \\ &\times [\mathrm{K}_0(kR_s)\mathrm{I}_1(kR) + \mathrm{I}_0(kR_s)\mathrm{K}_1(kR)] \\ &\times [\mathrm{K}_0(kR_s)\mathrm{I}_0(kR) - \mathrm{I}_0(kR_s)\mathrm{K}_0(kR)] \\ &+ k^4R^2R_s^2\,[\mathrm{K}_0(\mathrm{k}R_s)\mathrm{I}_1(kR) + \mathrm{I}_0(kR_s)\mathrm{K}_1(kR)]^2 \\ &- k^4R^2R_s^2\,[\mathrm{K}_0(kR_s)\mathrm{I}_0(kR) - I_0(kR_s)\mathrm{K}_0(kR)]^2\,. \end{aligned} \tag{3.3}$$

Here, I_n and K_n are the order n modified Bessel functions of the first and second kind respectively. The resulting dispersion curves for the parameters of the experiments 8 (case I) and 4 (case II) are shown in figure 9.

Experiment	F	μ (poise)	$\gamma_1^e(\mathrm{s}^{-1})$	γ_1^e/γ_m	γ_1^e/γ_1^t	Case
1	3.25	11.8	1.91	0.77	0.78	I
2	3.01	23.0	0.76	0.59	0.81	II
3	2.59	23.0	0.72	0.56	0.92	II
4	2.47	11.8	1.61	0.64	1.00	II*
5	2.33	23.0	0.70	0.55	1.01	II
6	1.94	11.8	1.74	0.72	0.96	II
7	1.73	23.0	0.98	0.82	0.82	I
8	1.73	23.0	1.12	0.94	0.99	I*
9	1.46	11.8	1.98	0.92	0.96	I
10	1.29	11.8	1.74	0.87	0.92	I
11	1.25	23.0	1.11	1.10	1.11	I
12	1.19	23.0	0.71	0.72	0.97	II
13	0.77	23.0	0.64	0.98	1.10	I
14	0.66	23.0	0.63	1.16	1.16	I
15	0.66	23.0	0.52	0.96	1.02	I
16	0.61	23.0	0.33	0.68	0.91	II
17	0.38	23.0	0.25	1.08	3.30	II
18	0.21	23.0	0.08	1.18	1.49	II

TABLE 2. Dimensionless film thickness and viscosity of each experiment. The measured growth rate of the primary mode for the early (linear) stage is denoted by γ_1^e, while γ_1^t is the prediction from the linear theory. The corresponding theoretical maximum growth rate is γ_m. The asterisk (*) indicates experiments reported in detail.

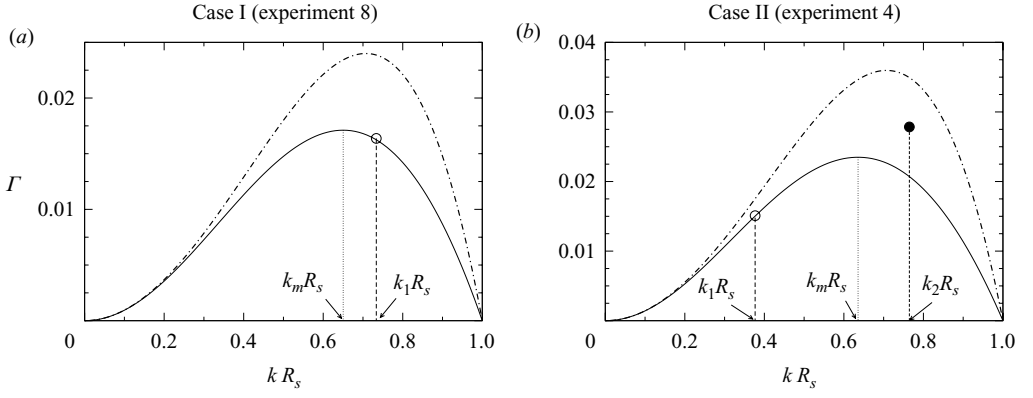

FIGURE 9. Dispersion curves given by the linear stability analysis (solid lines, (3.1)) for (*a*) case I (experiment 8) and (*b*) case II (experiment 4). The wavenumber of maximum growth rate, k_m, is represented by the vertical dotted line. The values of the *measured* growth rates for the experimental wavenumbers k_1 and k_2 are shown as open and closed circles, respectively. The dot-dashed lines, real part of (3.4), correspond to the longwave approximation by Craster & Matar (2006).

An alternative simpler expression in the limit of long wavelengths was obtained by Craster & Matar (2006) as

$$\Gamma = \frac{1}{16}(kR_s)^2\left(k^2R_s^2-1\right)\left(G^4-4G^2+3+\ln G\right) - \mathrm{i}Bo\frac{kR_s}{2}\left(G^2-1-2\ln G\right), \quad (3.4)$$

where $G = R/R_s = 1/(1+F)$. Because the Bond number $Bo \ll 1$ in our experiments, the imaginary part of Γ corresponding to convection can be safely neglected here. The

comparison between both approaches for the real part of Γ is also shown in figure 9. Clearly, the longwave approximation yields higher growth rates with the maximum shifted to a larger wavenumber. Note that the measured values of λ_1 may fall in a region where this approximation is not strictly valid (see figure 9*a*). Thus, we will only use the exact linear model by Goren (1962) for comparison with our experimental results. Instead, other authors, such as Smolka *et al.* (2008), used the approximation in (3.4) to compare with their experiments which included an important axial flow rate.

Usually it is assumed that the wavelength, λ_m, corresponding to the maximum growth rate, Γ_m, for the linear theory predicts the average distance between primary drops. For instance, in experiment 8 reported in § 2.1 we find $\lambda_1 = 0.89\lambda_m$ (see figure 9*a*). Note that in this experiment the value of λ_2 ($< \lambda_1$) falls in the stable region of the spectrum ($k_2 R_s > 1$). Therefore, its secondary maxima are not predicted by the linear theory and thus they are a consequence of nonlinear effects. The existence of this maxima is due to the decrease of the adjacent minima and not due to an increase of the fluid thickness at these peaks (see figure 4).

On the other hand, in experiment 4 (case II) the distance between primary peaks is always greater than λ_m. Here, we find $\lambda_1 = 1.69\lambda_m$, which has a theoretical growth rate, Γ_1, significantly lower ($\approx 36\,\%$) than the maximum one, Γ_m. Instead, we observe that the distance between secondary peaks, λ_2, is close to λ_m. Unlike the secondary peak in case I, here it corresponds to a very unstable linear mode. Thus, we expect that its growth rate is somehow related to the linear prediction. Note that now this peak is due to a genuine increase of the fluid thickness at the local maxima (see figure 6*b*). On the contrary, the wavenumber of the tertiary peaks falls in the stable region of the dispersion curve and the peaks become apparent, just because of a decrease of the adjacent minima, and not to a real increase of the thickness there, analogous to the secondary mode in case I.

Notwithstanding that one cannot predict λ_1 as the wavelength of maximum growth rate given by the linear stability analysis, λ_m, this theory correctly describes the observed growth rate γ_1^e at the early linear stage. The dimensionless experimental growth rates, Γ_1^e, (see figure 8*a* and table 2) are plotted as ordinates of the respective abscissa $k_1 R_s$ in figure 9 (open circles), and we obtain a very good agreement with the linear theory. Most of the experiments show similar behaviour with $\Gamma_1^e \approx \Gamma_1^t$ within a 10 % range. Notable exceptions to this results are the last two experiments in table 2, which correspond to the smallest values of F. The reason for this discrepancy is twofold: we lose resolution in the measurement of variations of a very thin film, and the instability enters very fast into the nonlinear regime. Therefore, these two last values of γ_1^e are less reliable. This hints that the measurement of growth rates may be more involved than that of the wavelength.

Even though the linear theory predicts a negative growth rate for λ_2 in case I (stable mode), we observe a growing peak for experiment 8 (see figure 8*b*). Thus, the evolution of this secondary maximum is out of the reach of the linear analysis, and it is an entirely nonlinear effect. In turn, the secondary peak in experiment 4 (case II) has a positive theoretical growth rate as in the experiment, but the value obtained from the best-fit line is $\approx 30\,\%$ larger. This suggests that the observed growth is a mixture of linear and nonlinear effects. Note, in passing, that within the linear theory, $\gamma(\lambda_2)$ is close to γ_m. In general, the measured growth rates of the secondary mode for experiments in case II depart from the corresponding linear theory predictions by up to 45 %. It is usually very difficult to measure these growth rates because their amplitudes are very small and the duration of the exponential growth behaviour is very short.

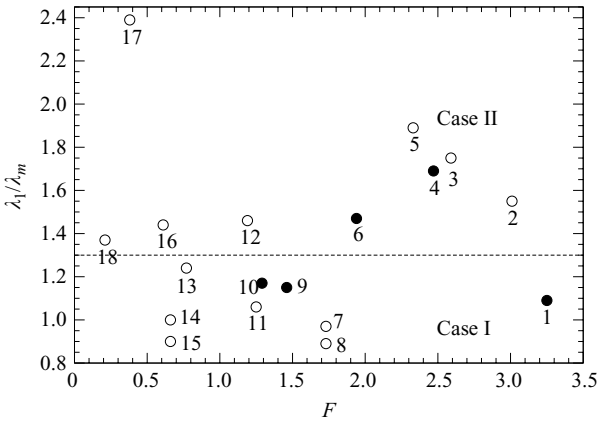

FIGURE 10. Ratio between the wavelength of primary mode, λ_1, and that of the maximum growth rate according to the linear theory, λ_m, versus the dimensionless film thickness, F. The open and closed circles correspond to $\mu = 23$ poise and 11.8 poise, respectively. When this ratio ≈ 1, the situation is that of case I, while for significantly greater ratios (> 1.3) the instability behaves as in case II. The lack of correlation between this ratio and F suggests that the selection of λ_1 is not governed by F.

In summary, the secondary peaks in experiments of case I (case II) correspond to stable (unstable) secondary modes. Therefore, a given experiment belongs to case I provided that

$$\lambda_2 < \lambda_c, \tag{3.5}$$

where $\lambda_c = 2\pi R_s$ is the critical (marginal) wavelength of the linear theory, and vice versa to case II (see table 1). This expression has not yet a predictive value, because it requires the knowledge of λ_2, which can only be measured after the secondary mode has grown enough (under either case I or case II). Because experimental evidence suggests that $\lambda_1 = 2\lambda_2$ (see figure 7), the above criterion can be put in terms of the primary peak wavelength as

$$\lambda_1 < 2\lambda_c. \tag{3.6}$$

This is confirmed by observing the last four columns in table 1, where the last column has been obtained by analysing the time evolution of the secondary peaks as in § 2.1 and 2.2.

In order to be able to predict if a given experiment belongs to case I or case II by observing only the distance between primary peaks, λ_1 (which is the easier parameter to measure), we give the following *rule of thumb*. Because for the range of F in the experiments $\lambda_c \approx 0.65\lambda_m$, we have that

$$\lambda_1 < 1.3\lambda_m \tag{3.7}$$

is the condition for case I, and vice versa for case II. In figure 10, we show the ratio λ_1/λ_m as obtained from different dimensionless film thicknesses, F (see the second and sixth columns in table 1). By using (3.7), we obtain a classification in agreement with that in the last column of that table. The experiments with λ_1/λ_m around 1.3 are more difficult to classify because the secondary modes are marginally stable. Figure 10 also shows that the selection of λ_1 is not governed by F, in contrast to λ_m which is a function of F. These results suggest that the details of the initial condition, which are out of the range of optical detection, may play a role in the selection of λ_1.

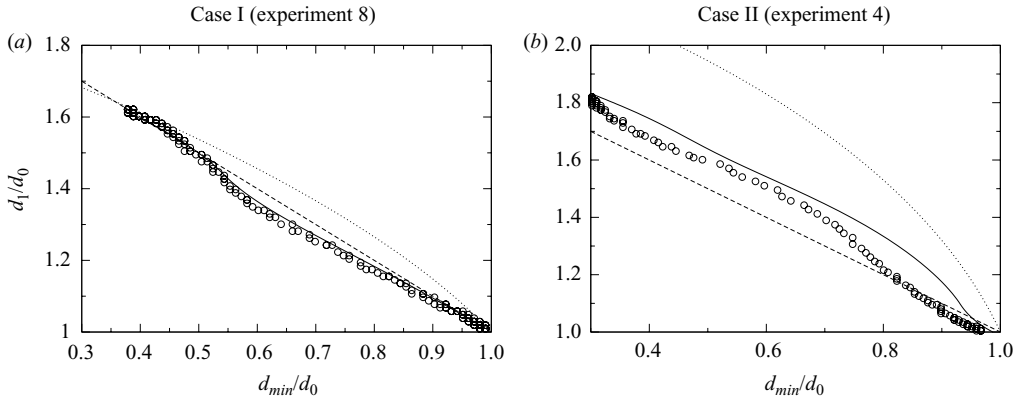

FIGURE 11. Maximum diameter, d_1, versus minimum diameter, d_{min}, as given by the quasi-static model by Goren (1964) ((4.1), dotted line). The circles correspond to experimental data and the solid line to numerical simulations of the Navier–Stokes equation (§ 5) using the experimental value λ_1. The dashed line corresponds to the simple model: $d_1/d_0 + d_{min}/d_0 = 2$.

4. Quasi-static model

When nonlinear effects saturate the growth rate, the linear predictions fail and another approach is needed. In the saturation stage, the kinematic effects are negligible and one can look for quasi-static state solutions for the shape of the free surface. This kind of model was also developed by Goren (1964) assuming that the system evolves into a series of bulges connected by cylindrical bridges. This assumption is based on his experimental observations where the secondary peaks were very small or not present at all. The model is based on a minimization of surface energy subject to the constraint of constant volume. The resulting variational principle yields a relationship between the radii of both the primary peak $h_1 = d_1/2$ and the bridge $h_{min} = d_{min}/2$, given by (see the Appendix)

$$\left(\frac{R_s}{h_1}\right)\left[\left(\frac{R_s}{h_1}\right)^2 - \cos^2\rho\right] = \left(\frac{\alpha}{3\pi}\right)\left[\left(2 + 3\cos\rho - \cos^2\rho\right) E_2\left(\frac{\pi}{2}, \sin^2\rho\right) - E_1\left(\frac{\pi}{2}, \sin^2\rho\right)\cos^2\rho\,(1 + 3\cos\rho)\right], \quad (4.1)$$

where $\alpha = 2\pi R_s/\lambda$, $\cos\rho = d_{min}/d_1$ and $E_1((\pi/2), \sin^2\rho)$, $E_2((\pi/2), \sin^2\rho)$ are elliptic integrals of the first and second kind, respectively.

The dotted lines in figure 11 correspond to d_1 versus d_{min} as given by this equation for experiments 8 (case I) and 4 (case II), respectively. Because the value of λ in this formulation is arbitrary, we choose the experimental distance between primary peaks, λ_1. Note that the curves have physical meaning for $d_{min} > D$, i.e. $d_{min}/d_0 > 1/(1 + F)$. The last point of this line corresponds to the solution given by de Gennes, Brochart-Wyart & Quéré (2004), where the bulges have the maximum possible height because no liquid bridge connecting them is considered. In these figures, we also plot the experimental values of d_1 and d_{min} obtained from the frames of the videos by capturing the neighbouring primary maxima and minima.

For case I, figure 11(a) shows that there is significant departure of Goren's curve with respect to the experimental points (circles), except very near the ending of the evolution. This is an evidence that the system cannot be modelled as a series of quasi-static states. This figure is similar to figure 2 of Goren (1964), but here we have

a better time resolution than in his experiments. Moreover, we use the measured local wavelength of the primary mode, λ_1, as λ in (4.1), while Goren used a fitting value which does not correspond to any particular experiment of his own.

Here, we propose another model based on the simple kinematic assumption that the decrease of the minimum is equal to the increase of the primary maximum. This yields a linear equation $2d_0 = d_1 + d_{min}$ (dashed line in figure 11) which nicely describes the experimental data. This is a good approximation not only for the initial linear stages but also for the nonlinear regime. The results of the numerical simulation described in § 5 are also shown in figure 11(*a*). The agreement with the experimental points is remarkable.

In case II, the results in figure 11(*b*) show larger discrepancy with the quasi-static model than that in the previous case. The origin of this departure is related to the existence of important secondary and tertiary maxima, which are neglected in this model. The correlation between the increase of the primary maximum and the decrease of the minimum is also broken when secondary maxima grow. Therefore, the symmetric kinematic assumption fails to give a good prediction of the main features of this case.

5. Numerical simulations

The previous models for the early and final stages provide a partial description of the instability, because they miss many important features of the problem, such as the appearance of secondary and tertiary peaks. Therefore, we perform nonlinear numerical simulations by employing a code that solves the full Navier–Stokes equations in axisymmetry for a viscous (Newtonian) and incompressible fluid. For our experiments, gravity effects can be neglected. The fluid velocity, $\boldsymbol{v}$, with radial and axial components v_r and v_z, respectively, is scaled with a characteristic velocity (Hammond 1983) $V = \sigma F^3/\mu$, the coordinates with fibre radius R, the time with R/V, the pressure p with σ/R, and the stress tensor $\boldsymbol{T}$ with $\mu V/R$. Thus, our equations in dimensionless form are

$$\nabla \cdot \boldsymbol{v} = 0, \tag{5.1}$$

$$\boldsymbol{T} = -p/F^3 \boldsymbol{I} + (\nabla \boldsymbol{v} + \nabla \boldsymbol{v}^{\mathrm{T}}), \tag{5.2}$$

$$Re\,[\partial \boldsymbol{v}/\partial \tau + \boldsymbol{v} \cdot \nabla \boldsymbol{v}] = \nabla \cdot \boldsymbol{T}, \tag{5.3}$$

with $Re = \rho R V/\mu = \rho R \sigma F^3/\mu^2$.

The following kinematic equation holds at the free surface:

$$(\boldsymbol{n} \cdot \boldsymbol{v})|_s = \boldsymbol{n} \cdot \dot{\boldsymbol{x}}_s, \tag{5.4}$$

where $(.)|_s$ indicates that the quantity is evaluated at the interface, $\boldsymbol{n}$ is the normal unit vector to the free surface, and $\dot{\boldsymbol{x}}_s$ represents the velocity of the points (nodes) lying on the interface that moves with the fluid velocity in the normal direction.

The numerical instability is triggered by imposing a slight perturbation to the uniform film that coats the fibre. For that purpose, a monomodal wave of small amplitude and wavenumber $k_1 = 2\pi/\lambda_1$ is employed in this section, because the linear approximation with λ_1 yields a good agreement with the growth rates observed in the experiments (see figures 8 and 11). Thus, the initial condition takes the form

$$r(z, t = 0)|_s = R_s + (R_s - R)\epsilon_0 \cos(k_1 z). \tag{5.5}$$

The parameter ϵ_0 is set to be sufficiently small to ensure that the instability grows in the so-called linear regime at the initial stages; usually, $\epsilon_0 = 10^{-3}$ is an appropriate value. Effects due to different choices of the initial conditions are discussed in § 6.

Because we consider a periodic disturbance, just a half wavelength needs to be solved; thus the boundary conditions at planes $z = 0$ and $z = \pi/k_1$ are

$$v_z = 0,\ \partial v_r/\partial z = 0,\ (\partial r/\partial z)|_s = 0. \tag{5.6}$$

At the wire surface, the no-slip condition is imposed. Only normal stresses are present at the free surface because the air is considered inviscid. The air pressure is used as a reference and, without loss of generality, set equal to zero; therefore, the stress balance at the interface results

$$\boldsymbol{n} \cdot \boldsymbol{T}|_s = \frac{\kappa}{F^3}\boldsymbol{n}, \tag{5.7}$$

where κ is the curvature of the surface.

The numerical technique considers a convenient spatial discretization by combining the Galerkin finite-element method with a suitable parametrization of the free surface by means of spines (Kistler & Scriven 1982; Khesghi & Scriven 1984). The physical domain is tessellated into quadrilateral elements. Biquadratic and bilinear interpolations are used to approximate the velocity and pressure fields, respectively. The weighted residuals are built in the usual form and a set of time-dependent ordinary differential equations results. This set is reduced to a system of nonlinear algebraic equations using a second-order finite-difference predictor–corrector scheme (Gresho, Lee & Sani 1980) and an adaptive step-size control method is implemented to march in time. The nonlinear algebraic system is linearized by mean of a Newton's algorithm, while the SuperLU routines (Demmel *et al.* 1999) are used to solve the linear system at each iteration.

The numerical code has been validated by Campana *et al.* (2004) to model the instability of a film coating the inner wall of a capillary tube. The results were successfully compared with a linear stability analysis (Goren 1962) and with experimental data obtained by Goldsmith & Mason (1963). An additional validation of the reliability of the code is achieved by comparing our simulations of the present problem with the results obtained by Mashayek & Ashgriz (1995). Only negligible differences in pinch-off times and interfacial shapes of the film for all cases treated by Mashayek & Ashgriz (1995) are found.

We choose the axial length of the domain as $\lambda_1/2$ to ensure that the simulation will eventually include all the meaningful wavelengths observed in the experiments. Without this consideration, one would be tempted to use instead half the wavelength of the maximum growth rate of the linear theory, $\lambda_m/2$, thus precluding the appearance of experimentally observed longer wavelengths.

5.1. *Simulation of case I*

In figure 4, we compare numerical and experimental timelines of consecutive primary and secondary maxima, as well as that of the local minimum for experiment 8. There is a remarkable agreement for the primary maximum and the minimum evolutions, which holds not only for the linear stage but also for the late saturation regime. On the other hand, the secondary maximum saturates *later* in the simulation than in the experiment. As a consequence, its numerical thickness is lower than the experimental one. This discrepancy is at most 5 % and is greater than the experimental error. As predicted by the linear theory, there is no growth of the secondary peak in both simulations and experiments.

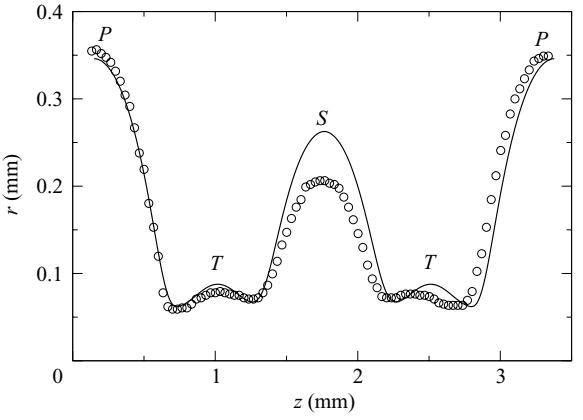

FIGURE 12. Numerical (solid line) and experimental (circles) interfacial profiles along the primary wavelength at $t = 3.3$ s (experiment 4, case II). The primary, secondary and tertiary peaks are indicated by P, S and T, respectively (see also figure 5.)

The numerical results of d_1/d_0 versus d_{min}/d_0 are also plotted in figure 11(a). The good agreement with the experimental points shows that the main geometrical features of the shape of the surface are well reproduced by the numerical simulation. In this experiment, the secondary mode is due to a nonlinear process that has only minor effects over the primary peak. This type of behaviour is characteristic of the experiments grouped in case I, where the secondary mode is linearly stable.

5.2. *Simulation of case II*

Here, we also find a good agreement between numerical predictions and experimental data for the primary maximum and minimum timelines (see figure 6a) corresponding to experiment 4. The behaviour of the secondary maximum is qualitatively well described by the simulation (see figure 6b). Unlike case I, the onset of the numerical secondary peak appears *before* the experimental one. Because this mode is strongly unstable in the linear regime (see figure 9b), the final saturated value of the secondary maximum is larger in the simulation than in the experiment. Nevertheless, the growth rates of both curves in the corresponding early and intermediate stages are very similar. Note that the secondary peaks are driven by nonlinear effects, but due to its linear instability the actual growth rate is a combination of both linear and nonlinear contributions.

The origin of the discrepancy between the simulated and actual evolutions of the secondary peak (see figure 6b) must be somehow related to the differences between the numerical and experimental shapes of the interfaces as shown in figure 12. There is an increase of the area of the experimental primary peak that implies a decrease of the amplitude of the secondary one respect to the numerical predictions. The larger width of the primary peak and the steepness of its slope could be a consequence of nonlinear injection of energy into short wavelength modes. However, this must be disregarded because finer grid simulations, which better describe small wavelength effects, yield very similar surface shapes.

In figure 6(c), we compare the timelines of the tertiary peak and the minimum from experiments and simulations. The onset time of this maximum is well predicted by the simulation. The tertiary maximum has the typical behaviour of stable linear

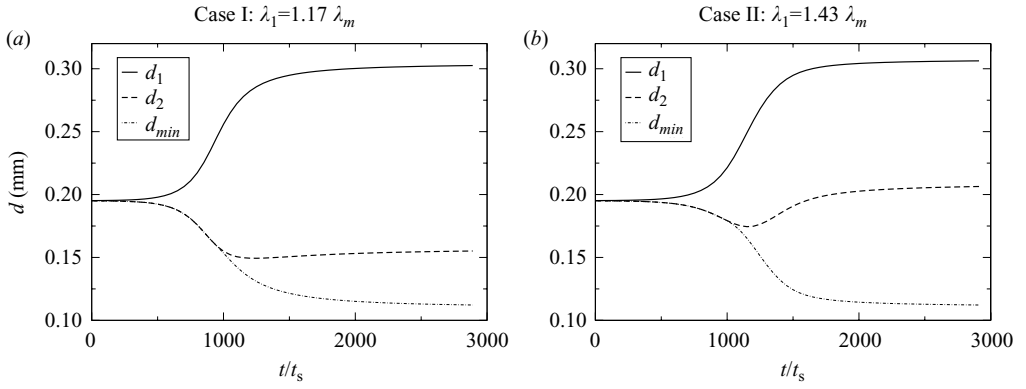

FIGURE 13. Numerical simulation of the time evolution of the amplitude of the modes in experiment 13 for λ_1 (*a*) below and (*b*) above 10 % of $1.3\lambda_m$. Time is scaled by $t_s = V/R$. The results confirm the criterion given by (3.7).

modes, which do not grow but remain flat as a plateau. This scenario is similar to that observed for the secondary maximum in case I.

Note that the tertiary mode may be affected by gravity in an indirect way. During the formation stage of the tertiary peaks, there may be convection of developed primary and secondary beads (i.e. large amplitude peaks) which leads to differences in the evolution of downstream and upstream tertiary peaks. Additional simulations including gravitational effects, not reported here for brevity, show that a better agreement for the tertiary maximum is achieved when this lack of symmetry is taken into account. Note that gravity effects are not relevant in the formation stage of primary and secondary peaks.

5.3. *Numerical generation of cases I and II*

Here, we aim to numerically confirm the *rule of thumb* given by (3.7) with respect to the prediction on the behaviour of the secondary mode corresponding to either case I or case II. Thus, for several values of F in the range of the experiments, we calculate the numerical evolution of the instability by perturbing the flow with a given value of λ_1. This wavelength is selected to be either above or below $1.3\lambda_m$, so that we expect to find a secondary mode that behaves as case II or case I, respectively. Figure 13 shows the numerical evolution of the amplitudes as obtained for $F = 0.77$ (as in experiment 13 in table 1) assuming λ_1 below and above 10 % of $1.3\lambda_m$. We note that for the smaller λ_1, d_2 does not grow as expected for case I. On the contrary, the larger λ_1 leads to a growing d_2, with a short exponential behaviour followed by saturation, as described for case II. Additional computations, not shown for brevity, confirm this trend.

6. Effects of initial conditions

Because it is difficult to ascertain the initial state of the actual small amplitude perturbations that trigger the instability in the experiments, we study the influence of the initial conditions on the evolution and final state of the system by using a numerical code.

As an approach to the hypothesis of the linear analysis, it is assumed that the sliding drop leaves a uniform film of thickness F, over which eventual disturbances evolve. The latter can be represented by a linear combination of a large number of modes of infinitesimal amplitude. In the simulation, only a finite number of modes with very

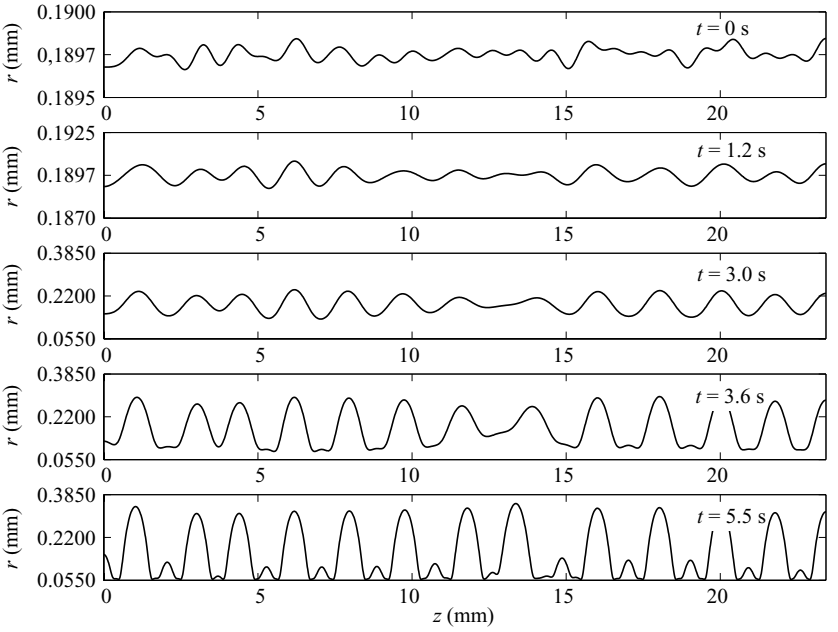

FIGURE 14. Radii of the interface profiles for a numerical experiment.

small finite amplitude can be used. Thus, the interfacial disturbance is expressed as

$$r(z, 0) = R_s + (R_s - R)\epsilon_0 \sum_{i=1}^{N_m} \beta_i \cos(k_i z), \tag{6.1}$$

where $k_i = k^{max}/N_m i$ is the wavenumber of the ith mode, and k^{max} and N_m are the maximum wavenumber and maximum number, respectively, of modes of the disturbance. The parameter $\epsilon_0 \ll 1$ is the maximum admissible amplitude of the modes (relative to the initial thickness), and $-1 \leqslant \beta_i \leqslant 1$ is a random number. Different multimodal disturbances are constructed by changing the random seed for β_i and setting $\epsilon_0 = 10^{-4}$, $k^{max} = 2k_m$ and $N_m = 50$. We also use periodic boundary conditions at the end of the computational domain.

In figure 14, we show interfacial shapes at different times for experiment 4 (case II). Because the maximum initial peak-to-peak amplitude of the disturbance ($\sim 0.5\,\mu$m for $t = 0$) is below the transverse resolution of the optical system (2.9 μm pixel^{-1}), this initial perturbation would not be detected experimentally. Only for $t > 1.2$ s (second graph in figure 14) the perturbation would become visible. We finish the simulation when the interface reaches a predefined minimum dimensionless thickness $h = 0.05$.

Figure 15 shows the discrete Fourier spectra of the corresponding interfacial profiles. In the first part of the evolution ($t \leqslant 3$ s), the amplitude of modes with $k_i R_s > 1$ and $k_i \ll k_m$ is quickly damped. Only modes in a region around k_m remain excited with growing amplitude, which agrees with the linear theory. Because the modes close to k_m have similar growth rates to Γ_m, they will be amplified with similar speeds. This can be seen for $t = 1.2$ s and $t = 3$ s in the second and third graphs of figure 15, which show that the relative amplitudes of the modes close to k_m are not significantly different. This is because all these modes have similar growth rates close to Γ_m. After $t = 3.6$ s, a secondary mode appears, whose wavenumber is very close to $2k_m$, analogous to what is observed in the experiments.

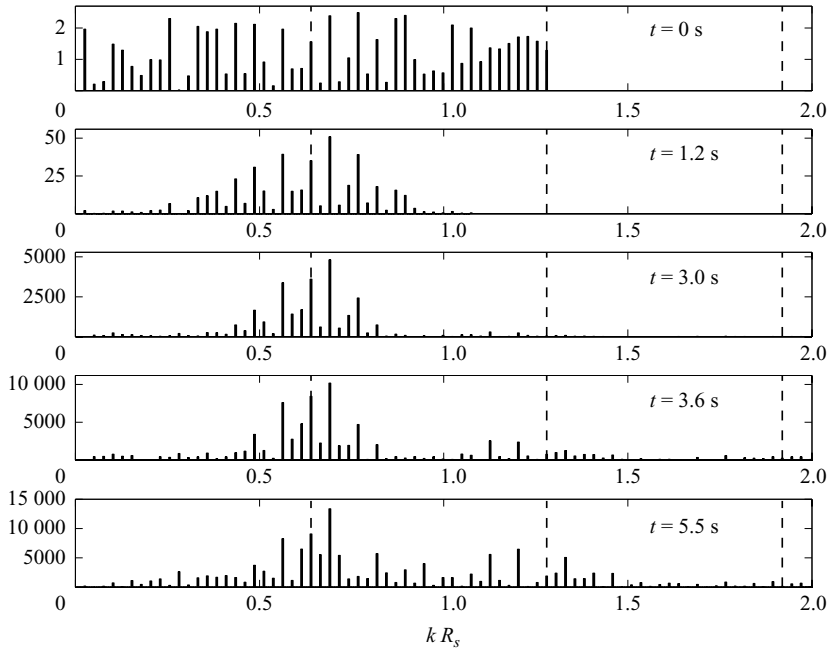

FIGURE 15. Fourier's power spectra corresponding to the interface profiles in figure 14. The vertical dashed lines, from left to right, indicate k_m, $2k_m$ and $3k_m$.

However, these results cannot explain the selection of the primary mode in experiment 4 and those in case II (cf. figure 10), where the primary mode differs up to 80 % of k_m. This suggests that the actual experimental set-up can generate imperceptible perturbations which excite modes with wavenumber closer to k_1. Therefore, the most unstable mode predicted by the linear theory would not dominate the evolution.

The following numerical experiments show a hypothetical situation in which this occurs. We consider experiment 4 (case II) with three initial perturbation spectra centred around k_1 and different widths. In figure 16, we show the Fourier power spectra for three different interfacial disturbances at $t = 0$ (first column) and $t = 1.2$ s (second column). From top to bottom, the disturbances at $t = 0$ for a given power have more localized spectra around the primary mode k_1 and, correspondingly, larger amplitude. In the three cases, the maximum initial amplitude of the perturbation is below the optical resolution of the experimental system, and therefore, at $t = 0$ the free surface would look practically flat. At $t = 1.2$ s, the amplitudes of the interfacial waves are large enough to be registered by an eventual optical system. In case (a), which has the most diffused initial spectra, the maximum at $t = 1.2$ s is very close to the most unstable mode predicted by the linear theory, k_m. On the other hand, cases (b) and (c), which have narrower spectra around k_1 lead to maxima closer to k_1, so that the observable wavenumber will strongly differ from k_m.

The simulations suggest that the primary mode can differ from the theoretical most unstable mode even though the initial perturbations are small enough for the linear theory to hold. Note that if a certain mode with wavenumber k_1 (different to k_m) is excited with large enough amplitude (relative to the others modes), the mode with k_1

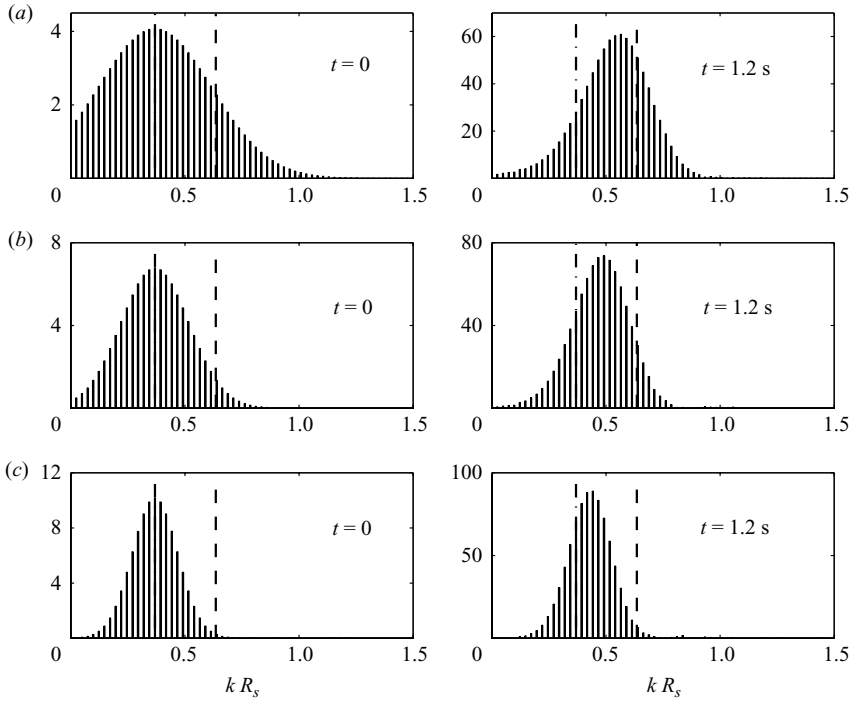

FIGURE 16. Numerical experiment with excited modes centred around k_1. We show the evolution of the Fourier spectra of the interfacial disturbances for different initial perturbations. The spectra have less dispersion around k_1 from (*a*) to (*c*). In all figures, the vertical dashed line at left indicates $k_1 R_s$, and the right one, $k_m R_s$.

will prevail over the one with k_m and it will be observed as the experimental dominant mode.

7. Conclusions

We report two different behaviours of the evolution of the instability, namely case I and case II. We find that the basic distinction between them depends on the behaviour of the evolution of the secondary peaks of the instability. The analysis reported here for a large set of experiments allows us to discriminate between both cases in terms of the wavelength of the primary peaks, instead of the time evolution of the secondary ones. This yields the simple condition: $\lambda_1 < 1.3\lambda_m$ for case I and vice versa for case II.

In case II, the secondary mode significantly grows and becomes comparable with the primary mode (see e.g. experiment 4 in table 1). This is because the linear growth rate of the secondary mode is larger than γ_1^e.

In case I, there is a secondary mode with small amplitude which is a consequence of nonlinear effects appearing when the primary mode has grown enough. In general, λ_1 is close to λ_m in a 20–30 % range. Only when $\lambda_1 \approx \lambda_m$ the final pattern shows a series of main beads separated by an average distance as that suggested by using the criterion of maximum growth rate in the linear theory.

Even though the secondary mode in case II is also a consequence of nonlinear effects, it grows practically with the maximum growth rate of the linear theory because λ_2 is close to λ_m. Therefore, it is sometimes difficult to distinguish between

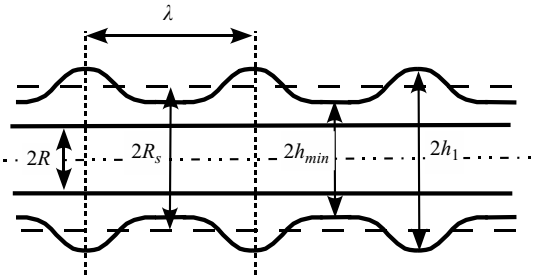

FIGURE 17. Sketch of the instability as assumed by the quasi-static model by Goren (1964).

primary and secondary beads in the final pattern. Only the detailed observation of the evolution allows us to determine which bead has evolved from a primary mode and which bead from a secondary one. As a conclusion, we note that the mere observation of the average distance between adjacent beads of comparable amplitude in the final pattern can be misleading because of the uncertainty to distinguish a primary bead from a secondary bead.

We acknowledge support from Agencia Nacional de Promoción Científica y Tecnológica (ANPCyT, Argentina) through grant PICTR 00094/2002. The authors are researchers of Consejo Nacional de Investigaciones Científicas y Técnicas de la República Argentina (CONICET).

Appendix. Minimal energy: Goren's solution

In order to obtain a quasi-static solution, Goren (1964) studied a minimal energy problem. He took a portion of fluid between two consecutive peaks (see figure 17). In his approach no secondary peak was considered. The symmetry of this problem allows us to restrict the analysis to the region $0 < z < \lambda/2$. Because the model is quasi-static, kinetic energy is negligible and only the surface tension effects are taken into account. The surface energy is proportional to

$$S = 2\pi \int_0^{\lambda} r\sqrt{1+r'^2}\,\mathrm{d}z = 2\pi \int_{r_{max}}^{r_{min}} r\sqrt{1+z'^2}\,\mathrm{d}r, \tag{A 1}$$

and it should be minimized with the constant volume constraint

$$V = \pi \int_0^{\lambda} r^2\,\mathrm{d}z = \pi \int_{r_{max}}^{r_{min}} r^2 z'\,\mathrm{d}r. \tag{A 2}$$

The problem can be solved using the Euler–Lagrange equations with the functional

$$F[r, z(r), z'(r)] = r\sqrt{1+z'^2} + \beta r^2 z',$$

where β is the Lagrange multiplier. Note that $\partial_z F = 0$ and, in consequence, $\partial_{z'} F = const$. This allows the first integration

$$\frac{rz'}{\sqrt{1+z'^2}} + r^2\beta = const. \tag{A 3}$$

We use the maximum radius, $d_1/2$, as the characteristic length, so that the non-dimensional variables are $X = 2z/d_1$, $Y = 2r/d_1$ and $\tilde{\beta} = 2h_1\beta$. The boundary conditions at the tip of the bulge are $Y'(0) = 0$ and $Y(0) = 1$. This allows us to rewrite

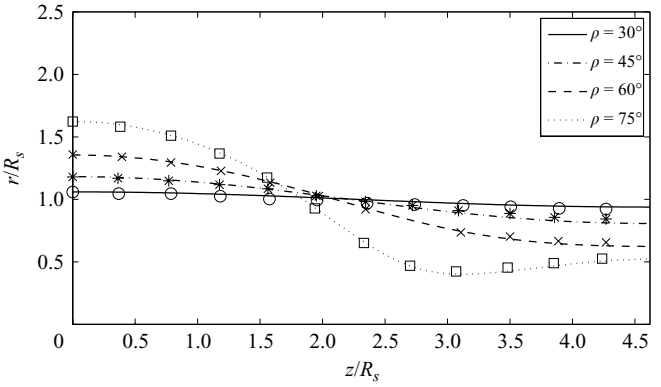

FIGURE 18. Comparison between simulation (lines) and experimental interfacial shapes registered by Goren (1964) (symbols).

(A 3) as

$$X'^2 = \gamma^2(1 + X'^2), \quad \gamma \equiv \frac{\tilde{\beta} - 1}{Y} - \tilde{\beta}Y. \tag{A 4}$$

By solving X' as a function of γ (i.e. Y), we obtain the following relationship:

$$X' = -\frac{|\gamma|}{1 - \gamma^2}. \tag{A 5}$$

Note that $X' < 0$ for $0 < X < X_0$, because the peak is at $X = 0$, and the thickness should decrease to reach its minimum value at $X = X_0$, where the plateau between bulges begins. From that point to $z = \lambda/2$ there is no change in r. Using the expression for γ given in (A 4), we obtain

$$X' = \frac{\mathrm{d}X}{\mathrm{d}Y} = -\frac{|1 - kY^2|}{\sqrt{(1 - Y^2)(k^2Y^2 - 1)}}, \tag{A 6}$$

with $k = 1 - 1/\tilde{\beta}$. The return points are $Y = 1$ at the peak, and $Y = 1/k = d_{min}/d_1$ at $X = X_0$. We now make the following change of variables:

$$Y^2 = 1 - \sin^2\rho \sin^2\psi. \tag{A 7}$$

where $\cos\rho = 1/k$. The point $X = X_0$ is given by the condition $Y = \cos\rho = d_{min}/d_1$ (or $\psi = \pi/2$). The integration of (A 6) leads to

$$X = \cos\rho E_1(\Phi, \sin^2\rho) - E_2(\Phi, \sin^2\rho), \tag{A 8}$$

where

$$E_1(\Phi, \sin^2\rho) = \int_0^{\Phi} \frac{1}{\sqrt{1 - \sin^2\rho \sin^2\psi}} \mathrm{d}\psi, \quad E_2(\Phi, \sin^2\rho) = \int_0^{\Phi} \sqrt{1 - \sin^2\rho \sin^2\psi}\, \mathrm{d}\psi$$

are the elliptic functions of the first and second type, respectively. The point X_0 corresponds to $\Phi = \pi/2$. The region $\lambda/2 < z < \lambda$ could be treated analogously using symmetry arguments. Now, it is possible to evaluate the total volume V by considering the expressions of z and r as a function of Φ. The value of V is that of the original flat coating in the considered portion. The final result is given in (4.1). Note that the corresponding equation in Goren's original paper is not properly written.

To check the validity of his approximation, Goren measured the interfacial shape of the annular coating by taking photographs of the instability with an experimental set-up similar to described in § 2. By comparing his experimental and theoretical results, Goren obtained a reasonable agreement for the interfacial shape of the film, except for his thickest coating ($F = 2.12$ over a wire of $d = 152.4\,\mu\text{m}$). For this case, he observed a *satellite drop* (secondary lobe) in the later stages of the evolution, which obviously cannot be predicted by his theory. Goren argued that such satellite drop could be caused by kinetic effects or gravity drainage. The appearance of such secondary lobe in Rayleigh instability over annular films is a very well documented process today and it can be predicted using both evolution equations for the interfacial profile (Gauglitz & Radke 1988) and more accurate numerical simulations (Mashayek & Ashgriz 1995). In figure 18, we show a comparison between our numerical solution and the experimental data of Goren. A very good agreement between both results for all stages of the evolution is observed. This points out that the appearance of the secondary lobe in Goren's experiment is not a consequence of gravity drainage but of the dynamics, which cannot be captured by this quasi-static model.

REFERENCES

de Bruyn, J. R. 1997 Crossover between surface tension and gravity-driven instabilities of a thin fluid layer on a horizontal cylinder. *Phys. Fluids* **9** (6), 1599–1605.

Campana, D. M., Di Paolo, J. & Saita, F. A. 2004 A 2-D model of Rayleigh instability in capillary tubes: surfactant effects. *Intl J. Multiphase Flow* **30** (5), 431–454.

Carroll, B. J. & Lucassen, J. 1974 Effect of surface dynamics on the process of droplet formation from supported and free liquid cylinders. *Chem. Soc. Faraday Trans.* **70**, 1228–1239.

Collicott, S. H., Zhang, S. & Schneider, S. P. 1994 Quantitative liquid jet instability measurement system using asymmetric magnification and digital image processing. *Exp. Fluids* **16**, 345–348.

Craster, R. V. & Matar, O. K. 2006 On viscous beads flowing down a vertical fibre. *J. Fluid Mech.* **553**, 85–105.

Demmel, J. W., Eisenstat, S. C., Gilbert, J. R., Li, X. S. & Liu, J. W. H. 1999 A supernodal approach to sparse partial pivoting. *SIAM J. Matrix Anal. Appl.* **20** (3), 720–755.

Duprat, C., Ruyer-Quil, C., Kalliadasis, S. & Giorgiutti-Dauphine, F. 2007 Absolute and convective instabilities of a viscous film flowing down a vertical fiber. *Phys. Rev. Lett.* **98**, 244502.

Frenkel, A. L., Babchin, A. J., Levich, B. G., Shlang, T. & Sivashinsky, G. I. 1987 Annular flows can keep unstable film from breakup: nonlinear saturation of capillary instability. *J. Colloid Interface Sci.* **115**, 225–233.

Gauglitz, P. A. & Radke, C. J. 1988 An extended evolution equation for liquid film breakup in cylindrical capillaries. *Chem. Engng Sci.* **43**, 1457–1465.

de Gennes, P. G., Brochart-Wyart, F. & Quéré, D. 2004 *Capillarity and Wetting Phenomena*. Springer.

Goldsmith, H. L. & Mason, S. G. 1963 The flow of suspensions through tubes. II. Single large tubes. *J. Colloid Sci.* **18**, 237–261.

Goren, S. 1962 The instability of an annular thread of fluid. *J. Fluid Mech.* **12**, 309–319.

Goren, S. 1964 The shape of a thread of liquid undergoing breakup. *J. Colloid Science* **19**, 81–86.

Goucher, F. S. & Ward, H. 1922 The thickness of liquid films formed on solid surfaces under dynamic conditions. *Phil. Mag.* **44**, 1002–1014.

Gresho, P. M., Lee, R. L. & Sani, R. L. 1980 On the time-dependent solution of Navier–Stokes equation in two and three dimensions. In *Recent Advances in Numerical Methods in Fluids*, vol. 1, pp. 27–79. Pineridge Press.

Hammond, P. S. 1983 Nonlinear adjustment of a thin annular film of viscous fluid surrounding a thread of another within a circular cylindrical pipe. *J. Fluid Mech.* **137**, 363.

Kalliadasis, S. & Chang, H.-C. 1994 Drop formation during coating of vertical fibres. *J. Fluid Mech.* **261**, 135–168.

Kapitza, F. S. & Kapitza, S. P. 1964 Experimental study of undulatory flow conditions (1949). In *Collected Papers of P. L. Kapitza*, pp. 690–709. Macmillan.

Khesghi, H. & Scriven, L. E. 1984 Penalty finite element analysis of unsteady free surface flows. *Finite Elements Fluids* **5**, 393–434.

Kistler, S. F. & Scriven, L. E. 1982 *Coating Flow Computations*. Applied Science Publishers.

Kliakhandler, I. L., Davis, S. H. & Bankoff, S. G. 2001 Viscous beads on vertical fibre. *J. Fluid. Mech.* **429**, 381–390.

Krantz, W. B. & Zollars, R. L. 1976 The linear hydrodynamic stability of film flow down a vertical cylinder. *AIChE J.* **22**, 930–938.

Lin, S. P. & Liu, W. C. 1975 Instability of film coating of wires and tubes. *AIChE J.* **21** (4), 775–782.

Lister, J. R., Rallison, J. M., King, A. A., Cumming, S. L. J. & Jensen, O. E. 2006 Capillary drainage of an annular film: the dynamics of collars and lobes. *J. Fluid Mech.* **552**, 311–343.

Mashayek, F. & Ashgriz, N. 1995 Instability of liquid coatings on cylindrical surfaces. *Phys. Fluids* **7** (9), 2143–2153.

Plateau, J. 1873 *Statique expérimentale et théorique des liquides soumis aux seules forces moléculaires*. Gauthier-Villars.

Quéré, D. 1990 Thin films flowing on vertical fibres. *Europhys. Lett.* **13** (8), 721–726.

Quéré, D. 1999 Fluid coating on a fibre. *Annu. Rev. Fluid Mech.* **31**, 347–384.

Rayleigh, Lord 1879 On the capillary phenomena in jets. Appendix I. *Proc. R. Soc.* **29** (A), 71.

Rayleigh, Lord 1892 On the instability of a cylinder of viscous liquid under capillary force. *Phil. Mag.* **34**, 145.

Smolka, L. B., North, J. & Guerra, B. K. 2008 Dynamics of free surface perturbations along an annular viscous film. *Phys. Rev.* E **77**, 036301.

Solorio, F. J. & Sen, M. 1987 Linear stability of a cylindrical falling film. *J. Fluid Mech.* **183**, 365–377.

Trifonov, Y. Y. 1992 Steady-state travelling waves on the surface of a viscous liquid film falling down on vertical wires and tubes. *AIChe J.* **38** (6), 821–834.

Weinstein, S. J. & Ruschak, K. J. 2004 Coating flows. *Annu. Rev. Fluid Mech.* **36**, 29–53.

Yarin, A. L., Oron, A. & Roseneau, P. 1993 Capillary instability of a thin liquid film on a cylinder. *Phys. Fluid* A **5** (1), 91–98.